



Article

Facile Synthesis of Polypyrrole-Functionalized CoFe₂O₄@SiO₂ for Removal for Hg(II)

Yuhao Zhao ¹, Kai Xia ¹, Zhenzong Zhang ¹, Ziming Zhu ¹, Yongfu Guo ^{1,2,*}  and Zan Qu ^{2,3}

¹ School of Environmental Science and Engineering, Suzhou University of Science and Technology, Suzhou 215011, China; 1713022014@post.usts.edu.cn (Y.Z.); 1713022009@post.usts.edu.cn (K.X.); 1713022013@post.usts.edu.cn (Z.Z.); 1513022025@post.usts.edu.cn (Z.Z.)

² Jiangsu Provincial Key Laboratory of Environmental Science and Engineering, Suzhou University of Science and Technology, Suzhou 215011, China; quzan@sjtu.edu.cn

³ School of Environmental Science and Engineering, Shanghai Jiao Tong University, Shanghai 200240, China

* Correspondence: yongfuguo@mail.usts.edu.cn; Tel.: +86-512-6809-2987

Received: 31 January 2019; Accepted: 7 March 2019; Published: 19 March 2019



Abstract: In order to avoid using toxic or harmful operational conditions, shorten synthesis time, enhance adsorption capacity, and reduce operational cost, a novel magnetic nano-adsorbent of CoFe₂O₄@SiO₂ with core-shell structure was successfully functionalized with polypyrrole (Ppy). The physical and chemical properties of CoFe₂O₄@SiO₂-Ppy are examined by various means. The as-prepared CoFe₂O₄@SiO₂-Ppy nanomaterial was used to adsorb Hg²⁺ from water. During the process, some key effect factors were studied. The adsorption process of Hg²⁺ onto CoFe₂O₄@SiO₂-Ppy was consistent with the pseudo-second-order kinetic and Langmuir models. The Langmuir capacity reached 680.2 mg/g, exceeding those of many adsorbents. The as-prepared material had excellent regeneration ability, dispersibility, and stability. The fitting of kinetics, isotherms, and thermodynamics indicated the removal was endothermic and spontaneous, and involved some chemical reactions. The application evaluation of electroplating wastewater also shows that CoFe₂O₄@SiO₂-Ppy is an excellent adsorbent for Hg²⁺ ions from water.

Keywords: adsorbent; polypyrrole; heavy metal; mercury; modification

1. Introduction

Currently, with the enlargement of industrial production, an enormous amount of wastewater is discharged into water bodies, causing serious of pollution of soil, air, water, and other issues. Especially, the pollution of heavy metals resulting from industrial wastewater is increasingly severe [1]. Among them, mercury pollution is a unique issue, due to its highly toxicity, easy migration, and bioaccumulation in human beings [2,3]. Therefore, research on mercury removal is being actively carried out all over the world. In order to remove mercury from aqueous solution, adsorption technology, as a cost-effective method, is widely researched and used [4]. Among many adsorbents, magnetic nanomaterials are a novel functional material type with unique physical and chemical properties, the most critical of which is that it can easily achieve separation from water under an external magnet [5], which can significantly reduce the operational cost.

However, magnetic nanomaterials, such as Fe₃O₄, CoFe₂O₄, and MnFe₂O₄, have poor adsorption and selectivity for heavy metals in water [6–8]. The poor adsorption capacity is either inherent or due to distinctive characteristics. In addition, easy agglomeration and the absence of surface active functional groups also limit their adsorption properties. Fortunately, the properties of magnetic nanomaterials can be generally improved after modification [9,10]. Thus, more and more magnetic nanomaterials are being modified and then employed to remove various pollutants, including heavy metal ions.

CoFe₂O₄, a common magnetic nanomaterial, has the advantages of low toxicity and easy preparation and separation, and can be modified to not only improve its dispersibility in aqueous solution, but to also greatly enhance its stability.

A common coating modification is to coat CoFe₂O₄ particles with another coating layer (SiO₂, C or organodisulfide polymer, etc.) under the outer layer of CoFe₂O₄ particles [8,11]. The good dispersibility and stability of CoFe₂O₄ particles in water can be realized by coating modification. However, high-efficiency removal for heavy metal mercury cannot be achieved by coating modification alone. Therefore, the surface chemical performance of CoFe₂O₄ still needs to be further decorated to enhance the mercury adsorption ability. Grafting modification is a good method to improve the surface chemical performance of CoFe₂O₄ nanomaterials. Common grafting groups include -NH₂ [8,10], -SH [12,13], and others [14]. However, most of modification methods with -NH₂ and -SH usually are either too complicated or use toxic, harmful, or hazardous acetone [15] and toluene [16] as reaction media [17,18]. In addition, some literature employed nitrogen protection or high temperature to obtain grafting groups [7,8]. The above grafting methods are beneficial to increasing the removal ability for mercury ions, but unfortunately greatly increase the disposal cost. Moreover, it is more likely to cause secondary pollution. In order to avoid using toxic, harmful, or hazardous solvents, it is necessary to seek a safer and more economical material.

Polymers have been widely employed in materials science. Polymers can form complexes with other materials. During the process of forming complexes, some special functional groups can be introduced to carriers. Among the polymers, polypyrrole (Ppy) has the benefits of easy large-scale preparation, excellent stability, and low preparation cost [19]. It has been widely applied in many fields such as energy memory, drug transport, and super capacitors, etc. Ppy polymerizes from pyrrole monomers under the action of oxidizing agents and can encapsulate many materials. The presence of amine in the polymer backbone allows Ppy to be used as a favorable modifier. Based on our previous research, the magnetic graphene oxide grafted with Ppy had very high removal capacity for mercury (II) ions. The Langmuir capacity reached 400 mg/g at pH 7 [20].

Hence, in the present research, a novel nanomaterial (CoFe₂O₄@SiO₂-Ppy) with a core-shell structure was successfully synthesized through grafting with Ppy and was used to remove Hg²⁺ from water. The aim is to enhance the removal ability dispersibility, and stability of CoFe₂O₄ in water through optimizing its surface performance with a safe, economical, and facile synthesis method. Moreover, some key influence factors, including regeneration, were investigated. Meanwhile, the adsorption mechanism for Hg²⁺ was also investigated through a series of kinetic and equilibrium models.

2. Materials and Experimental Methods

2.1. Chemicals and Materials

Pyrrole (Py), sodium dodecyl benzene sulfonate (SDBS), cobaltous nitrate hexahydrate (CNH), iron acetylacetonate, ethylene glycol (EG), iron chloride hexahydrate (FeCl₃·6H₂O), sodium acetate anhydrous (CH₃COONa), polyethylene glycol, cetyltrimethylammonium bromide (CTAB), ammonia water (NH₃·H₂O, 25–28 wt.%), and tetraethyl silicate (TEOs) were all obtained from Aladdin Reagent (Shanghai, China). The chemicals were all analytical grade.

2.2. Preparation of Materials

CoFe₂O₄@SiO₂ was prepared based on our previous research report [13]. Briefly, a homogeneous solution with CNH (2.18 g), iron acetylacetonate (5.29 g), CH₃COONa (6.51 g), polyethylene glycol (2.0 g) and EG (90 mL) was placed in an autoclave (150 mL) to undergo a hydrothermal reaction at 453 K for 14 h, and then CoFe₂O₄ nanoparticle was generated.

CoFe₂O₄ (0.30 g) was dispersed in CTAB solution (0.15 g CTAB, 150 mL pure water) with sonication for 20 min. TEOs (1.0 mL) and NH₃·H₂O (1.3 mL) are dropped into the above reaction

system with mechanical stirring at 353 K for 3 h. Obtained materials were washed and then put into a muffle furnace and then calcined at 673 K for 4 h to obtain $\text{CoFe}_2\text{O}_4@\text{SiO}_2$ nanoparticles.

A certain amount of $\text{CoFe}_2\text{O}_4@\text{SiO}_2$ (0.15 g) and SDBS (0.025 g) were dissolved in 100 mL pure water with ultrasound treatment for 30 min and mechanical stirring was applied for 30 min. after that, 0.25 mL pyrrole solution was added slowly.

Subsequently, 10 mL of completely dissolved $\text{FeCl}_3 \cdot 6\text{H}_2\text{O}$ (3.0 g) was slowly added. The system reacted with mechanical stirring for 4 h. The Resulting product ($\text{CoFe}_2\text{O}_4@\text{SiO}_2\text{-Ppy}$) was rinsed 3 times and then desiccated at 338 K. The formation scheme of the pyrrole polymer is shown in Figure 1.

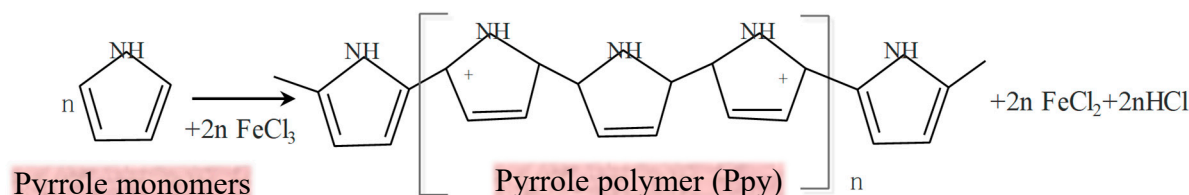


Figure 1. Formation scheme of Ppy with pyrrole monomers.

Figure 1 shows the polymerization scheme of pyrrole monomers to produce polypyrrole polymer. It can be seen that the byproduct hydrochloric acid is produced during the progress of reaction, which increases the acidity of the reaction medium. If CoFe_2O_4 is directly modified with Ppy, the nature of CoFe_2O_4 is bound to be greatly impacted during the course of the reaction. The reason is that magnetic CoFe_2O_4 has a cubic spinel structure [21] and easily agglomerates and can suffer from acid corrosion. Thus, the formation of silicon shells on the surface of CoFe_2O_4 by hydrolysis of TEOs has a protective effect [8].

2.3. Sample Characterizations

The values of surface area (BET) were decided by N_2 adsorption-desorption isotherms (Micromeritic TriStarII 3020, Norcross, GA, USA). The morphology was observed by scanning electron microscope (SEM) (FEL, Phenom, Hillsboro, OR, USA) and transmission electron microscopy (TEM) (JEM-2100F, Tokyo, Japan). X-ray Diffraction (XRD, D8 Advance, Bruker, Karlsruhe, Germany) analysis was applied to investigate the crystallization and phase. Functional groups were identified by Fourier transform infrared (FT-IR) spectrophotometry (Thermo, Nicolet-6700, Waltham, MA, USA). Magnetic strength was compared by vibrating sample magnetometry (VSM) (Quantum design, PPMS-9, San Diego, CA, USA). Elements compositions were confirmed by energy-dispersive spectrometry (EDS) and X-ray photoelectron spectroscopy (XPS) (Thermo Scientific, 250Xi, Waltham, MA, USA). The concentration of Hg^{2+} ions at any time t (min) was quantified using ICP-OES.

2.4. Batch Experiments

The solution containing a certain concentration of Hg^{2+} was prepared based on previous research report [13]. The adsorption capacities of $\text{CoFe}_2\text{O}_4@\text{SiO}_2\text{-Ppy}$ for Hg^{2+} were evaluated by initial solution pH, dosage, reaction time (t , min), solution temperature (T , K), and coexisting ions in the solution.

The effects of pH were evaluated by adding 0.1 mol/L hydrochloric acid and 0.1 mol/L sodium hydroxide solutions to adjust pH from 3 to 9. The test was performed for 8 h at 298 K by a 250 mL sealed conical flask with 100 mL Hg^{2+} solution and 5 mg adsorbent. The initial concentration (C_0) of Hg^{2+} was 40 mg/L.

The effect of adsorbent dosage was investigated by adding various adsorbents of 0.03, 0.05, 0.08, 0.1, and 0.15 g/L with $C_0 = 40$ mg/L, pH = 8 and $T = 298$ K. Contact time t was investigated at various time intervals of 3, 4, 5, 8, 10, 15, 30, 60, 90, 120, 240, 360, 480, 600, and 720 min with $C_0 = 40$ mg/L, dosage of 5 mg, pH = 8 and $T = 298$ K. Isotherms were investigated at 298 K, pH = 8, and $t = 8$ h with C_0 of 20, 30, 40, 50, 60, 80, and 100 mg/L.

The equilibrium capacity (q_e , mg/g) was investigated according to C_0 , equilibrium capacity (C_e , mg/g), dosage (g), and solution volume (L) [20]. The instantaneous capacity (q_t , mg/g) was investigated according to C_0 , instantaneous concentration C_t (mg/L), dosage (g) and solution volume (L) at any time (t , min) [13]. The removal efficiency (E , %) of Hg^{2+} ions was obtained based on initial concentration C_0 and equilibrium concentration C_e .

3. Results and Discussion

3.1. Characterization of Materials

Figure 2 reveals that pore diameters of $CoFe_2O_4$, $CoFe_2O_4@SiO_2$, and $CoFe_2O_4@SiO_2$ -Ppy only changed slightly after modification with the Barrett-Joyner-Halenda method. The values of both BET and the total pore volume of as-prepared $CoFe_2O_4@SiO_2$ -Ppy significantly increased to $218.56\text{ m}^2/\text{g}$ and $0.888\text{ cm}^3/\text{g}$, which are 4.5 and 2 times as large as $CoFe_2O_4$, respectively. The results not only show that the silicone shell was successfully wrapped on the outer surface of $CoFe_2O_4$, but also are conducive to enhancing the adsorption capacity of $CoFe_2O_4@SiO_2$ -Ppy.

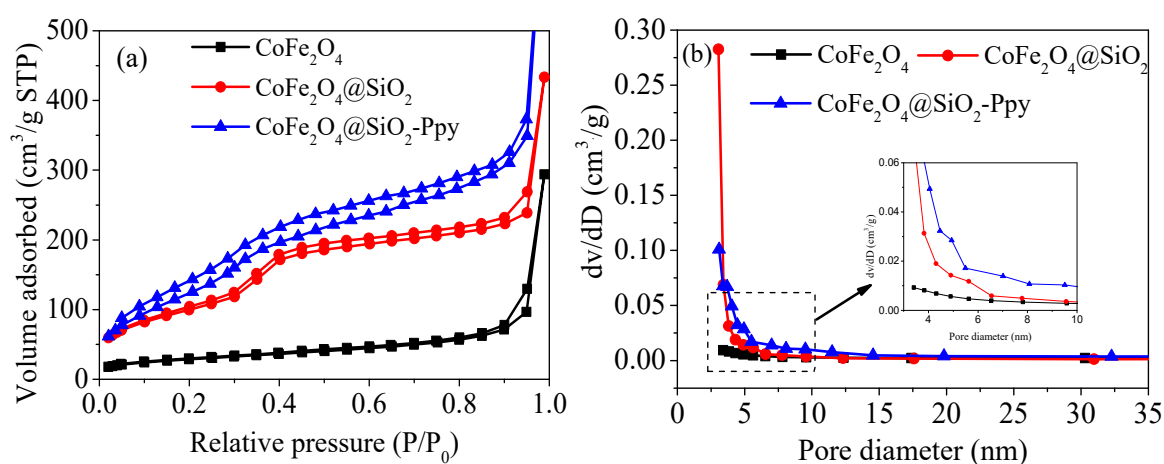


Figure 2. Adsorption-desorption plots (a); Size distribution (b).

In addition, the calcination of surfactant CTAB makes $CoFe_2O_4@SiO_2$ exhibit a porous fluffy morphology. The calculated values of BET, total pore volume, and pore diameter data are listed in Table 1.

Table 1. Structure of three adsorbents.

Samples	BET (m^2/g)	Total Pore Volume (cm^3/g)	Pore Diameter (nm)
$CoFe_2O_4$	48.49	0.424	3.413
$CoFe_2O_4@SiO_2$	225.36	0.552	3.062
$CoFe_2O_4@SiO_2$ -Ppy	218.56	0.888	3.106

A noteworthy point is that the BET value of $CoFe_2O_4@SiO_2$ -Ppy is reduced compared to $CoFe_2O_4@SiO_2$. This owes to the fact that lots of the chain-like Ppy packed on the surface of the material and sealed the porous mesh structure of the material during the continuous process of polymerization [22].

Figure 3 is the SEM and TEM patterns of $CoFe_2O_4$, $CoFe_2O_4@SiO_2$, and $CoFe_2O_4@SiO_2$ -Ppy. The corresponding particle diameters are about 50–90, 70–120, and 90–140 nm, respectively. For $CoFe_2O_4$, the reason of agglomeration may be mainly due to the magnetic dipole–dipole interaction [23].

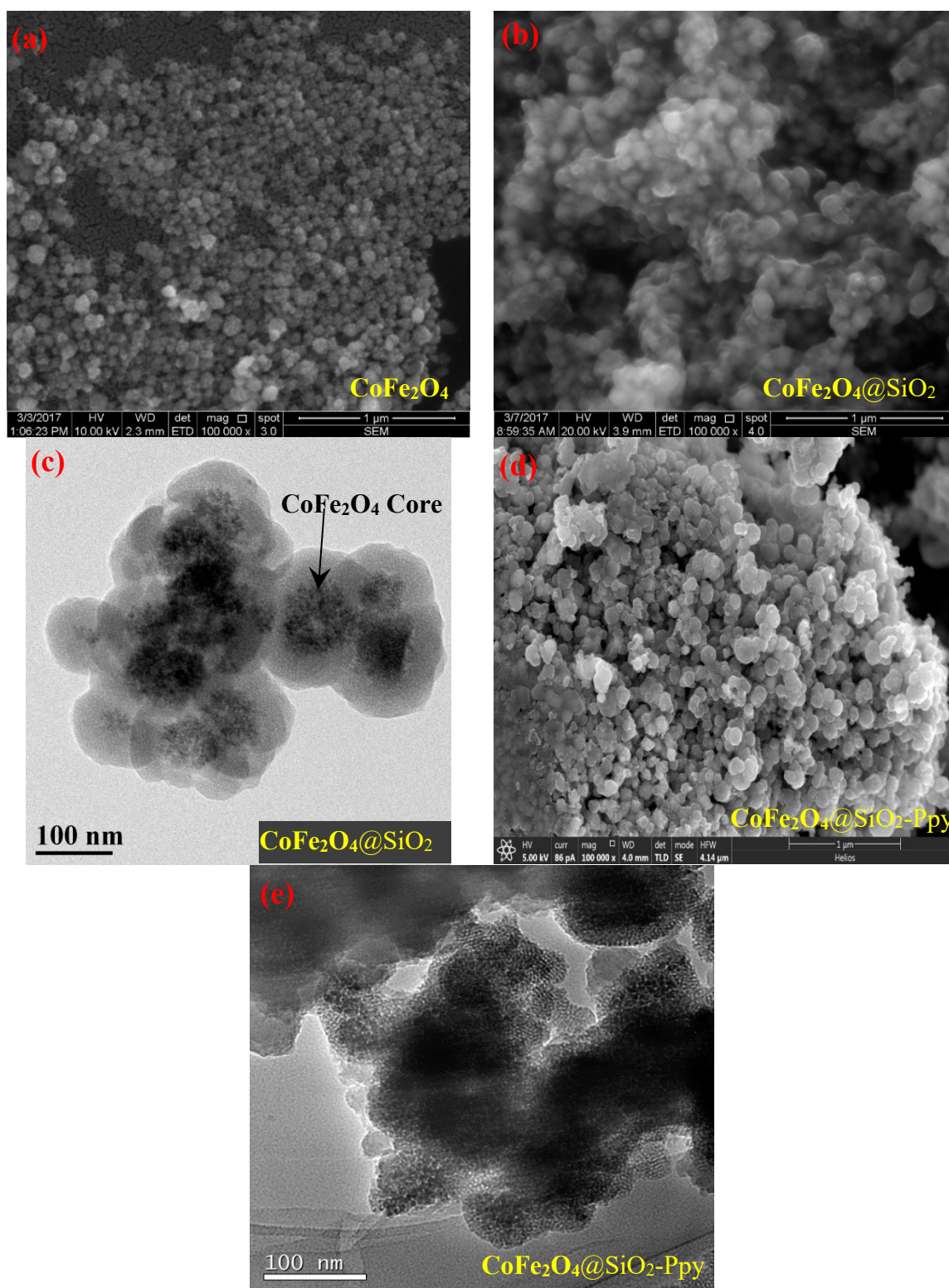


Figure 3. Scanning electron microscopy (SEM) of (a,b); Transmission electron microscopy (TEM) of (c–e) of the three as-prepared materials.

As shown in Figure 3b, the size of $\text{CoFe}_2\text{O}_4@\text{SiO}_2$ becomes larger compared to CoFe_2O_4 , proving that the silicon shell has successfully loaded on the surface of CoFe_2O_4 nanoparticles. However, most of the particles are still stuck together, resulting in a poor dispersibility. As shown in Figure 3c, the agglomeration of $\text{CoFe}_2\text{O}_4@\text{SiO}_2\text{-Ppy}$ decreases significantly, and it can be clearly observed that the

material has a smooth surface and a ball-like shape. From the TEM image of $\text{CoFe}_2\text{O}_4@\text{SiO}_2$ -Ppy shown in Figure 3d, it can be judged by different electron penetration: the black core is CoFe_2O_4 ; the lighter shell is a silicon shell (SiO_2 layer) and Ppy. The above results suggest that $\text{CoFe}_2\text{O}_4@\text{SiO}_2$ -Ppy has a core-shell structure and that $\text{CoFe}_2\text{O}_4@\text{SiO}_2$ has been enclosed into the Ppy matrix [24].

As shown in Figure 4, the EDS elemental analysis of $\text{CoFe}_2\text{O}_4@\text{SiO}_2$ -Ppy shows the peaks of Co, Fe, C, Si, and N and indicates the major constituents of magnetite, silice shell, and Ppy, which verifies the existence of CoFe_2O_4 , silice shell (SiO_2 layer), and Ppy. From Figure 5a–f, the material mainly contains Fe, N, O, Si, and Co. It shows that Ppy was successfully combined with $\text{CoFe}_2\text{O}_4@\text{SiO}_2$ and evenly distributed on the outer surface.

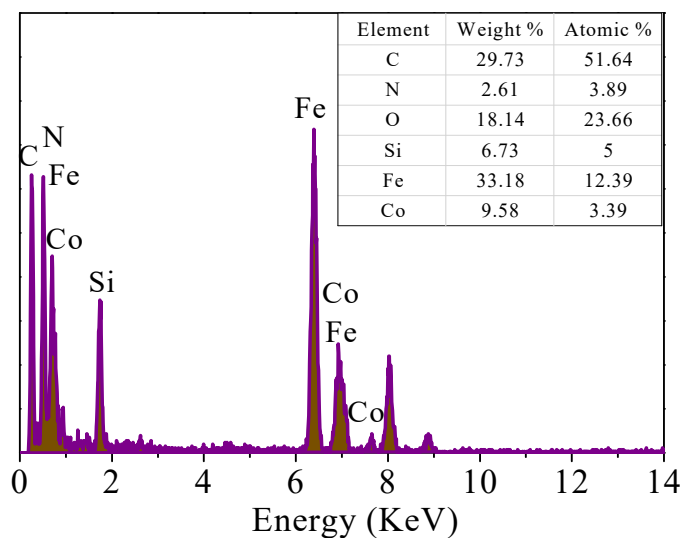


Figure 4. Energy-dispersive spectrometry (EDS) elemental analysis of $\text{CoFe}_2\text{O}_4@\text{SiO}_2$ -Ppy.

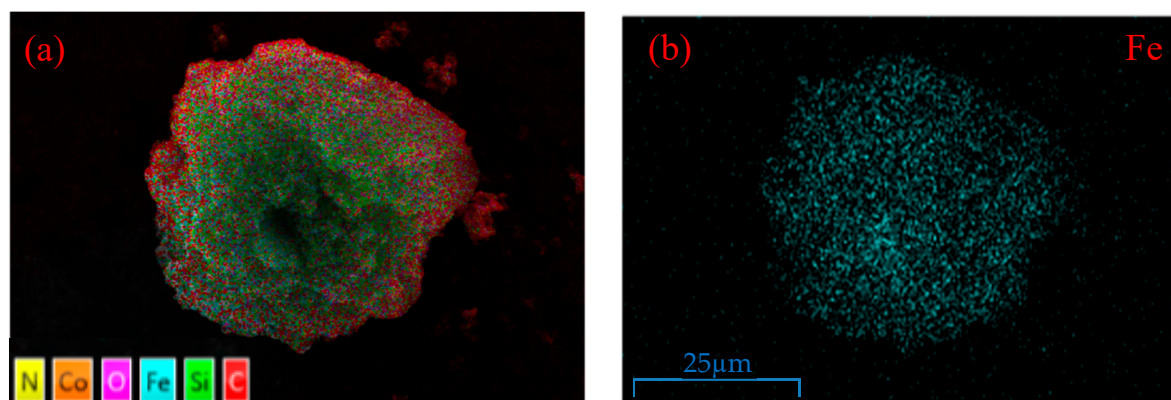


Figure 5. Cont.

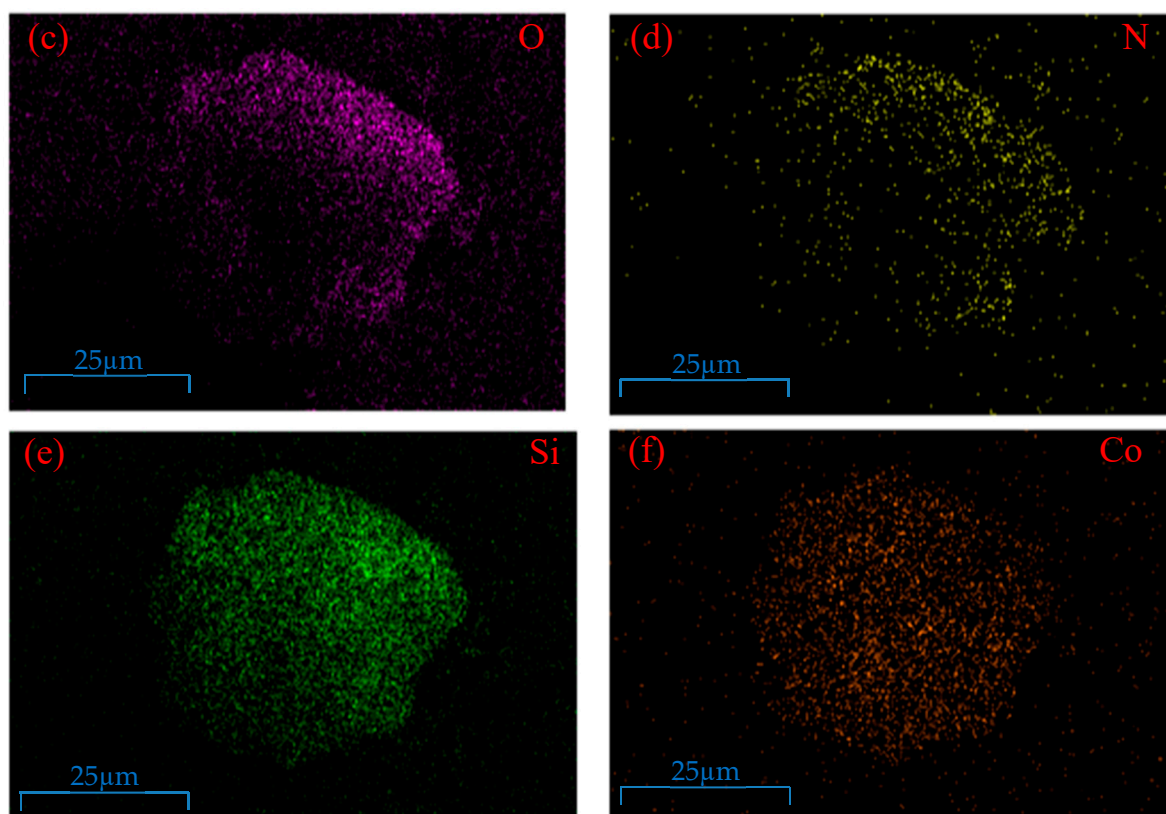


Figure 5. (a) SEM with X-ray area scanning; EDS mappings of (b) Fe, (c) O, (d) N, (e) Si, and (f) Co of $\text{CoFe}_2\text{O}_4@\text{SiO}_2\text{-Ppy}$.

Figure 6a shows the XRD images of as-prepared materials. For CoFe_2O_4 , the main six peaks correspond to the (220), (311), (400), (422), (511), and (440) planes [10,13], respectively.

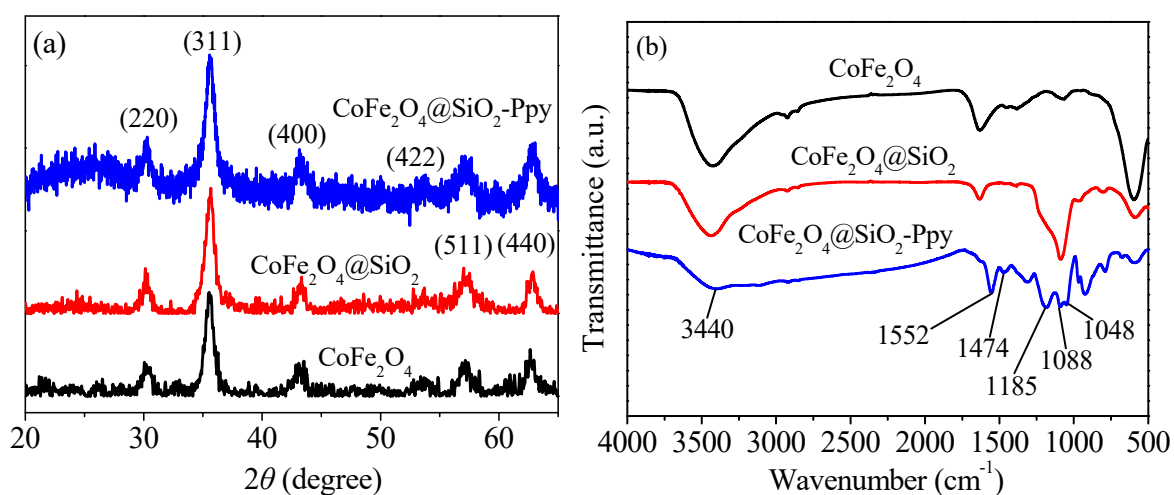


Figure 6. X-ray diffraction (XRD) images (a) and Fourier transform infrared (FT-IR) spectra (b).

The characteristic peaks in Figure 6a of the three as-prepared materials were accordant with the diffraction pattern of CoFe_2O_4 (JCPDS No. 22-1086) [25]. The diffraction peaks of $\text{CoFe}_2\text{O}_4@\text{SiO}_2$ covered by a silicon shell are consistent with those of CoFe_2O_4 , and the decrease in vibration intensity may be due to the influence of the encapsulated silicon shell.

No new peaks indicate that the crystal form of the material is not affected by the modification. In the pattern of $\text{CoFe}_2\text{O}_4@\text{SiO}_2\text{-Ppy}$, there is a wide peak at 2θ of about 25° , which is the characteristic peak of Ppy [26,27], probably due to a certain level of Ppy crystallization.

According to Figure 6b, a wide peak around at 3440 cm^{-1} can be found due to tensile vibration of the surface adsorbing $-\text{OH}$ in water [28]. The wide peak at 1088 cm^{-1} can be ascribed as Si-O-Si , indicating that there is successful attachment of a silicon shell (SiO_2 layer) on the outer surface of CoFe_2O_4 [29].

A bond at 1552 cm^{-1} is the proof of the existence of Ppy, corresponding to C=C vibration [30]. Peaks at 1185, 1048, and 474 cm^{-1} are C-H stretching in plane [31], C-H bending mode vibration in plane [32,33], and the vibration of C-N in a pyrrole ring [34]. The presence of these above functional group peaks indicates that Ppy is indeed present in the $\text{CoFe}_2\text{O}_4@\text{SiO}_2\text{-Ppy}$ composite.

The magnetic property of each material was detected by VSM, and the corresponding analytical data was plotted in Figure 7. Based on the hysteresis loop, the saturation magnetic moments are found to be 56.03, 44.68, and 15.46 emu/g . The magnetic reduction of $\text{CoFe}_2\text{O}_4@\text{SiO}_2$ may be because of the nonmagnetic silicon shell wrapped outside the magnetic core, which also indirectly demonstrates that the silicon shell has wrapped successfully.

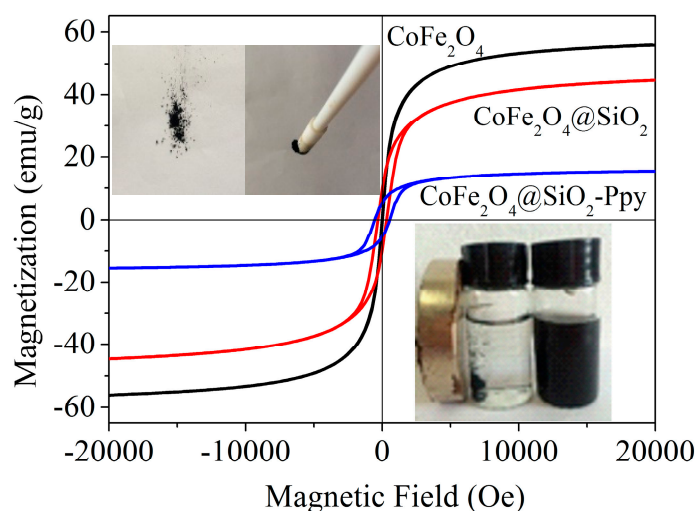


Figure 7. Vibrating sample magnetometry (VSM) analysis of the three as-prepared materials.

After Ppy loaded on the surface of $\text{CoFe}_2\text{O}_4@\text{SiO}_2$, the magnetic value has a significant decline from 44.7 to 15.5 emu/g . The reason is probably that a small number of magnetic particles in the composite are shielded by conductive Ppy [22,35]. Although the magnetic value of $\text{CoFe}_2\text{O}_4@\text{SiO}_2\text{-Ppy}$ is weak, it can still separate quickly from the water by an outer magnetic field. The inserted picture shows the effect of magnetic separation with an outer magnet.

From the wide-scan XPS spectra shown in Figure 8a, it can be seen that there are six peaks at 110.1, 293.7, 405.4, 541.2, 738.2, and 813.9 eV , attributed to $\text{Si } 2p$, $\text{C } 1s$, $\text{N } 1s$, $\text{O } 1s$, $\text{Fe } 2p$, and $\text{Co } 2p$, respectively. In the pattern of $\text{CoFe}_2\text{O}_4@\text{SiO}_2$, the peaks of Co , Fe , and C become weak and a new peak of $\text{Si } 2p$ appears at 110.1 eV .

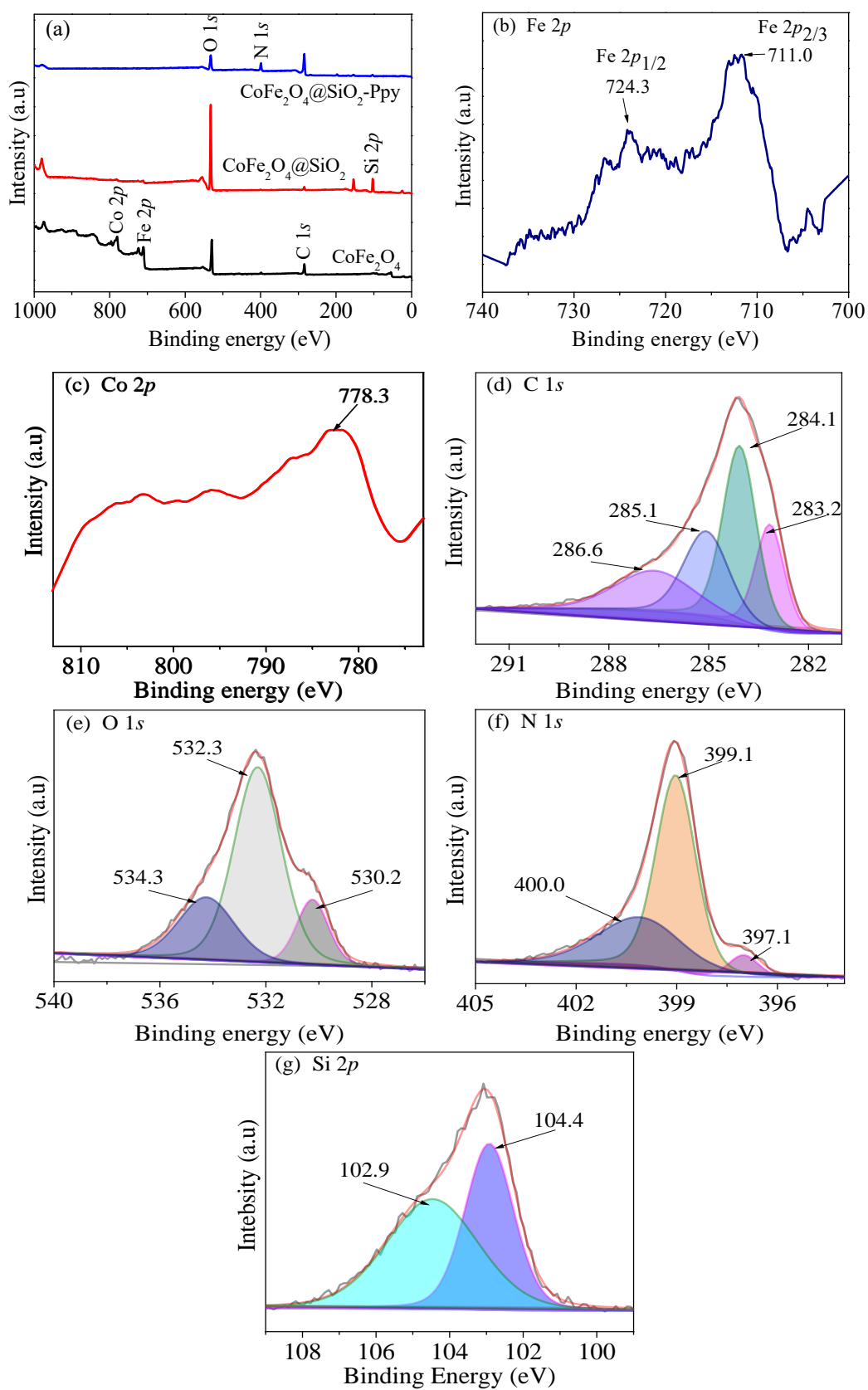


Figure 8. X-ray photoelectron spectroscopy (XPS) spectra of (a) survey scan; (b) Fe 2p, (c) Co 2p, (d) C 1s, (e) O 1s, (f) N 1s, and (g) Si 2p of CoFe₂O₄@SiO₂-Ppy.

Figure 8b,c indicates successful synthesis of CoFe_2O_4 nanoparticles in the as-prepared composite [13,20]. In Figure 8d, there are four C 1s peaks at 283.2, 284.1, 285.1, and 286.6 eV. The peaks at 284.1 and 285.1 eV are mainly attributed to β -carbons and α -carbons, respectively. The peak at 286.6 eV is assigned to C=N bonds [22,36].

The O 1s spectrum shown in Figure 8e has three peaks at 530.2, 532.3, and 534.3 eV. The peak at 530.2 eV is the oxygen in carbonyl group [13]. The peaks at 532.3 and 534.3 eV are related to the oxygen atoms in hydroxyl ions and water [10].

On the pattern of $\text{CoFe}_2\text{O}_4@\text{SiO}_2\text{-Ppy}$, the N 1s peaks shown in Figure 8f at 397.1, 399.1, and 400.0 eV are related to NH-, -N=, and N^+ , respectively [37]. The appearance of new peaks of N 1s indicates the successful polymerization of pyrrole monomers. The peaks of Si 2p in Figure 8g are located at 102.9 and 104.4 eV, proving that a silicon shell is formed on the surface of CoFe_2O_4 through TEOs hydrolysis.

It can be seen from the Figure 9 that the value of zero charge (pH_{zpc}) of $\text{CoFe}_2\text{O}_4@\text{SiO}_2$ is 6.8. When the pH is more than 6.8, the Zeta potential of $\text{CoFe}_2\text{O}_4@\text{SiO}_2$ is negative, indicating that SiO_2 has been coated on the surface of CoFe_2O_4 [12]. However, the small Zeta potential at pH 8 indicates that the $\text{CoFe}_2\text{O}_4@\text{SiO}_2$ solution has a poor stability.

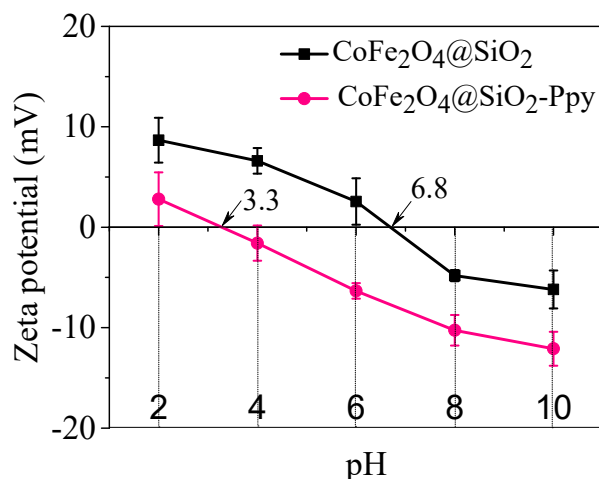


Figure 9. Zeta potentials of $\text{CoFe}_2\text{O}_4@\text{SiO}_2$ and $\text{CoFe}_2\text{O}_4@\text{SiO}_2\text{-Ppy}$.

After grafting with Ppy, the value of pH_{zpc} of $\text{CoFe}_2\text{O}_4@\text{SiO}_2\text{-Ppy}$ is decreased to 3.3, which owes to the existence of $-\text{NH}_2$ [38], proving a successful synthesis of $\text{CoFe}_2\text{O}_4@\text{SiO}_2\text{-Ppy}$. In addition, the Zeta potential of $\text{CoFe}_2\text{O}_4@\text{SiO}_2\text{-Ppy}$ is -12.1 mV at pH 8, which is far lower than that of $\text{CoFe}_2\text{O}_4@\text{SiO}_2$ of -6.2 mV. The result reveals that the solution of $\text{CoFe}_2\text{O}_4@\text{SiO}_2\text{-Ppy}$ is relatively stable, which is consistent with the data shown in Figure 3c. The results of low Zeta potential value and good stability are conducive to alleviating the agglomeration of adsorbent solution and enhancing the removal ability for positively charged Hg^{2+} ions.

3.2. Adsorption Performance Test

3.2.1. Influence of pH

It is well known that pH can affect the surface charges of adsorbents and the form of heavy metals [39]. As shown in Figure 10, $\text{CoFe}_2\text{O}_4@\text{SiO}_2$ has low adsorption capacity for mercury ions, only 98.4 mg/g at pH = 5. Compared to $\text{CoFe}_2\text{O}_4@\text{SiO}_2$, the adsorption capacity of $\text{CoFe}_2\text{O}_4@\text{SiO}_2\text{-Ppy}$ is greatly enhanced, and the adsorption plot has a rapid ascending tendency with the increasing pH. A basic equilibrium adsorption is reached at pH = 8 and achieves 420.8 mg/g. Therefore, pH = 8 was chosen as the reaction condition in later study.

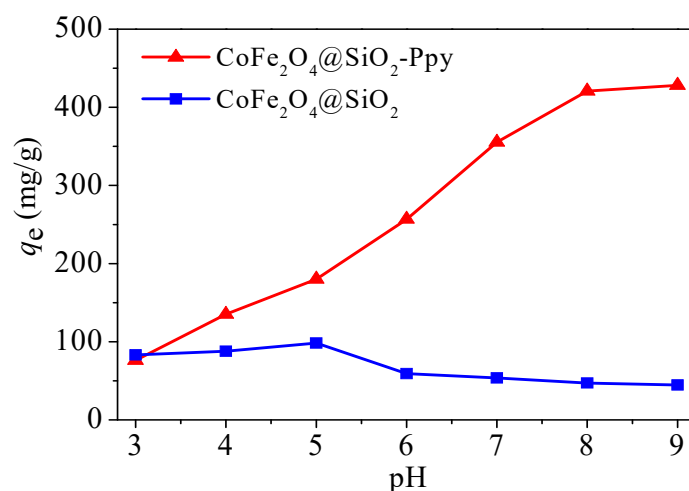


Figure 10. Effect of pH on removal capabilities of CoFe₂O₄@SiO₂ and CoFe₂O₄@SiO₂-Ppy.

3.2.2. Influence of Dosage

The capacity and efficiency (E) were investigated by changing the dosage of CoFe₂O₄@SiO₂-Ppy of 3, 5, 8, 10, and 15 mg with 100 mL 40 mg/L Hg²⁺ solution. As illustrated in Figure 11, as the dosage increases, the adsorption capacity shows a downward trend, but the removal efficiency increases. The dosage of 0.05 g/L is selected for subsequent test conditions.

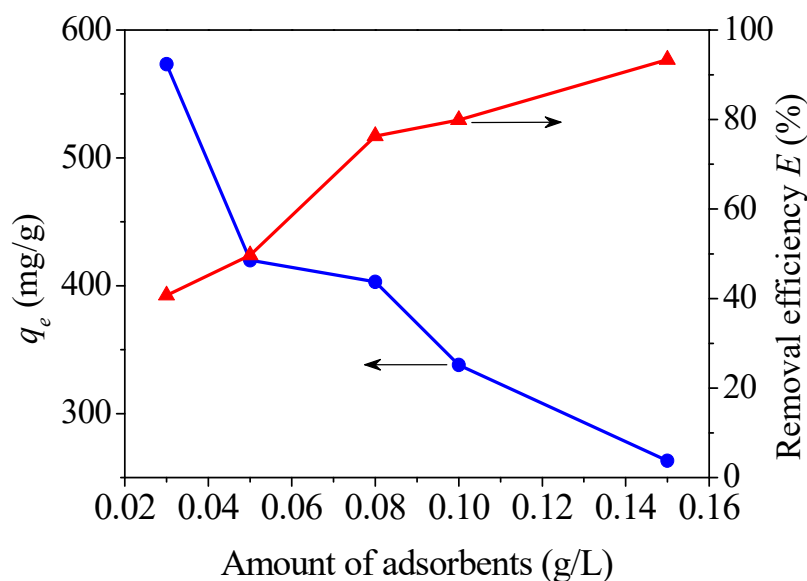


Figure 11. Effect of dosage with CoFe₂O₄@SiO₂-Ppy as adsorbent.

3.2.3. Influence of Adsorption Time

As shown in Figure 12a, adsorption capacity increases over time, but the growth rate is different in different periods. In the first hour, the growth of adsorption capacity is significantly fast and reaches the half of the adsorption equilibrium. The reason is that the adsorbent is in the form of powder with the particle diameter of 90–140 nm, so the distance from mercury ions to the surface active site of the adsorbent becomes shorter. In addition, the large BET value of CoFe₂O₄@SiO₂-Ppy provides lots of active sites for Hg²⁺. Simultaneously, the concentration gradient of Hg²⁺ between the solution and on the surface of CoFe₂O₄@SiO₂-Ppy is enough large, resulting in a quick gathering of Hg²⁺ onto CoFe₂O₄@SiO₂-Ppy.

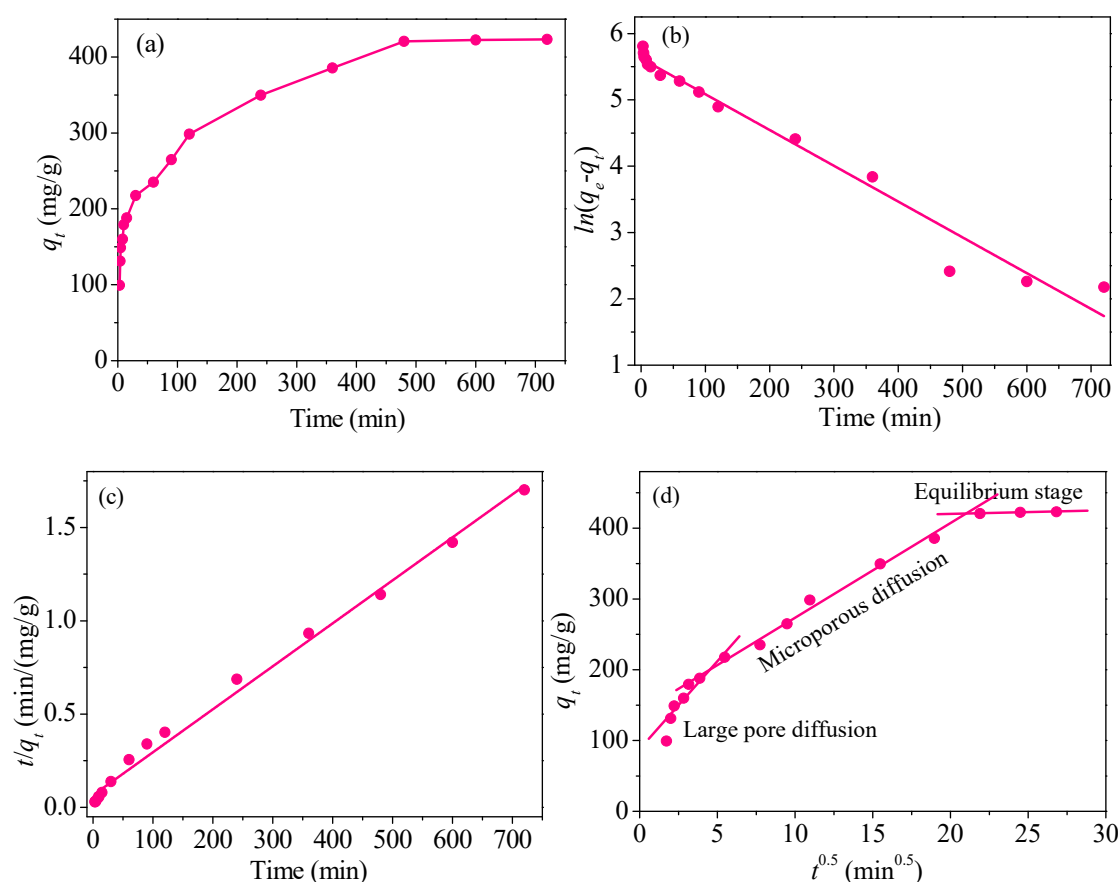


Figure 12. (a) Effect of contact time; results of (b) pseudo-first-order, (c) pseudo-second-order and (d) intraparticle diffusion.

Subsequently, with the reducing amount of available active sites and the concentration gradient, the adsorption rate slows. The adsorption equilibrium is reached after 8 h.

3.3. Adsorption Kinetics

To explore the possible reaction mechanism of $\text{CoFe}_2\text{O}_4@\text{SiO}_2\text{-Ppy}$, the pseudo-first-order, pseudo-second-order, and intraparticle diffusion kinetics models were employed to fit the test results. The pseudo-first-order:

$$\ln(q_e - q_t) = \ln q_e - k_1 t \quad (1)$$

The pseudo-second-order:

$$\frac{t}{q_t} = \frac{1}{q_e^2 k_2} + \frac{t}{q_e} \quad (2)$$

The intraparticle diffusion:

$$q_t = k_{di} t^{0.5} + C_i \quad (3)$$

here, k_1 (min^{-1}) and k_2 ($\text{g}/(\text{mg}\cdot\text{min})$) are rate coefficient; k_{di} ($\text{mg}/(\text{g}\cdot\text{min}^{0.5})$) represents diffusion rate coefficient. C_i (mg/g) is the thickness of the boundary layer. The test results were linearly fitted using the above three kinetic models and were shown in Figure 12b–d, and all the relevant results are listed in Table 2.

Table 2. Kinetic fitting results of Hg^{2+} onto $\text{CoFe}_2\text{O}_4@\text{SiO}_2\text{-Ppy}$.

Pseudo-First-Order				Pseudo-Second-Order				
$q_{e,\text{exp}}$ (mg/g)	$q_{e,\text{cal}}$ (mg/g)	k_1 (1/min)	R^2	$q_{e,\text{cal}}$ (mg/g)	k_2 (g/(mg·min))	R^2		
420.8	277.2	0.0054	0.970	434.8	0.00008	0.993		
Intraparticle Diffusion								
k_{d1} (mg/(g·min ^{0.5}))	C_1 (mg/g)	R_1^2	k_{d2} (mg/(g·min ^{0.5}))	C_2 (mg/g)	R_2^2	k_{d3} (mg/(g·min ^{0.5}))	C_3 (mg/g)	R_3^2
23.46	94.26	0.933	13.17	141.74	0.975	0.49	410.18	0.949

Regression coefficient (R^2) in Figure 12b,c shows that pseudo-second-order fitting has a higher R^2 compared with pseudo-first-order fitting with R^2 . Moreover, according to the calculated adsorption capacity ($q_{e,\text{cal}}$) in Table 2, the $q_{e,\text{cal}}$ in the pseudo-first-order fitting and pseudo-second-order fitting are 277.2 mg/g and 434.8 mg/g, respectively. The latter value is closer to the value $q_{e,\text{exp}}$ of 420.8 mg/g, indicating that pseudo-second-order fitting is more consistent with the adsorption process.

The adsorption process was fitted by the intraparticle diffusion model and plotted in Figure 12d. From Figure 12d, the adsorption process consists of three different adsorption phases: large pore diffusion phase, microporous diffusion phase, and equilibrium adsorption phase. At the first phase, the adsorption rate is the fastest; at the second phase, the rate becomes relatively slow, and tends to be gentle at the final phase of adsorption.

For further comparison of each linear fitted stage, the values of k_{di} and regression coefficients R^2 in each stage were calculated separately and listed in Table 2. Obviously, the coefficients k_{di} are in the order of $k_{d1} > k_{d2} \gg k_{d3}$, so the overall adsorption process with $\text{CoFe}_2\text{O}_4@\text{SiO}_2\text{-Ppy}$ as the adsorbent is mainly controlled by the first and second stages.

In the first stage, the concentration of Hg^{2+} is high and Hg^{2+} can quickly come into contact with the adsorbents. Numbers of unoccupied active sites provide favourable conditions for rapid adsorption. At the second stage, after almost all of the external activity sites are occupied, residual Hg^{2+} ions enter into the pores of $\text{CoFe}_2\text{O}_4@\text{SiO}_2\text{-Ppy}$ and then adsorb onto the inner surface of the pores [40]. Moreover, the adsorption capacity reaches 420.8 mg/g and approaches the adsorption equilibrium at the second stage.

Finally, the k_{d3} value of 0.49 mg/(g·min^{0.5}) represents a state of near-adsorption equilibrium. The R^2 obtained by the intraparticle diffusion model are not high, and the fitting line deviates from the origin, showing there are many factors existing during the process of adsorption.

3.4. Adsorption Isotherms

For the aim of further investigating the adsorption capacity of $\text{CoFe}_2\text{O}_4@\text{SiO}_2\text{-Ppy}$ on Hg^{2+} , the experimental data was treated by the Langmuir (Equation (4)) and Freundlich (Equation (5)) isotherms.

$$\frac{C_e}{q_e} = \frac{C_e}{Q_m} + \frac{1}{Q_m K_L} \quad (4)$$

here, Q_m and K_L represent maximum capacity (mg/g) and constant, respectively. The separation constant R_L can be used to represent that the type of isotherms [20].

$$\ln q_e = \ln K_F + \frac{1}{n} \ln C_e \quad (5)$$

The separation factor:

$$R_L = \frac{1}{1 + K_L C_0} \quad (6)$$

here, K_F and n represent the Freundlich constants. $1/n$ represents the uneven factor, commonly used to describe the deviation degree of the adsorption linearity.

The fitting results of two isotherm models are shown in Figure 13. The values of isotherm constant and R^2 for Langmuir and Freundlich are listed in Table 3. R^2 from Langmuir are over 0.99 and higher than Freundlich, indicating that the Langmuir fitting has good consistency with Hg^{2+} adsorption and the adsorption process is a molecule layer reaction. Moreover, chemical reaction may be the main effect factor [10]. R_L from Langmuir is between 0 and 1, illustrating a favorable isotherm.

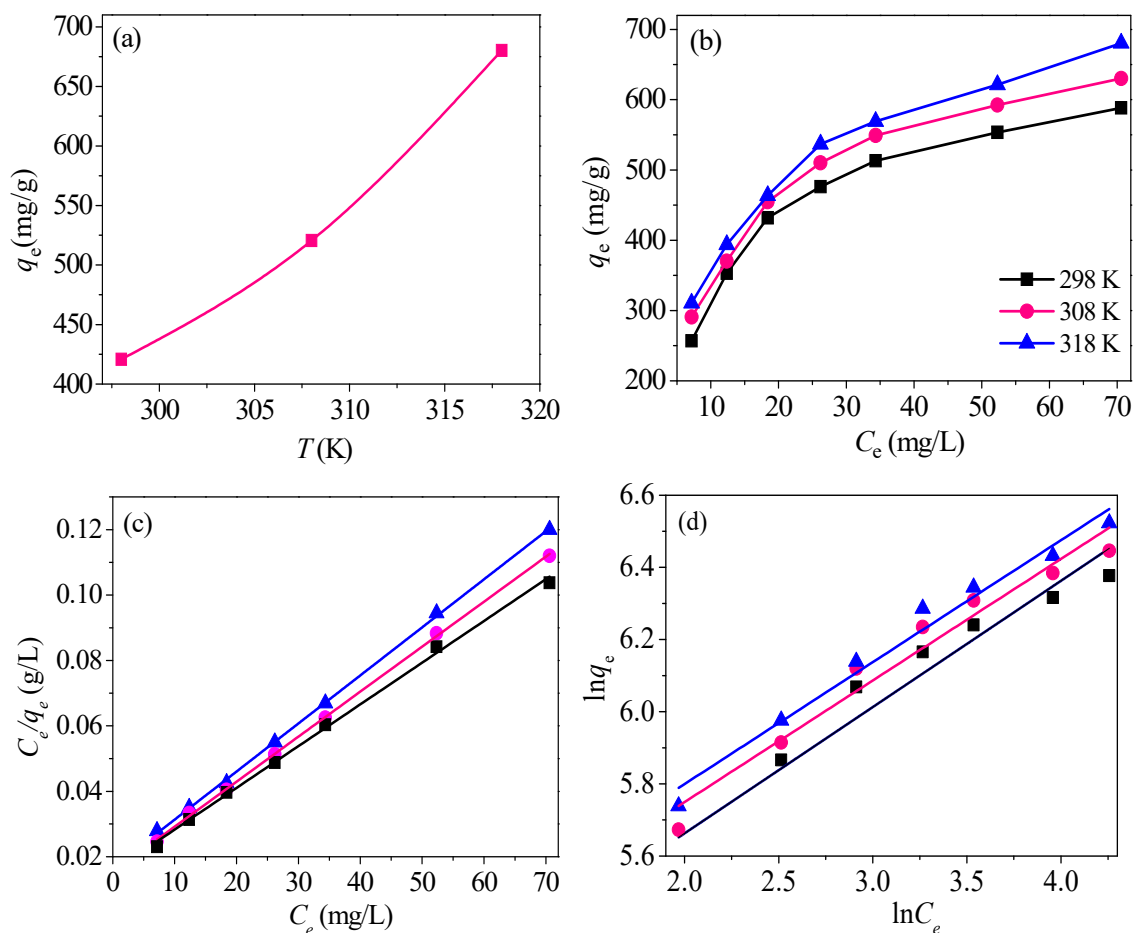


Figure 13. (a) Adsorption of Hg^{2+} under different temperatures; (b) adsorption isotherms; (c) Langmuir and (d) Freundlich isotherms of $CoFe_2O_4@SiO_2$ -Ppy.

Table 3. Isotherm data of $CoFe_2O_4@SiO_2$ -Ppy.

T (K)	Langmuir Isotherm			Freundlich Isotherm			
	Q_m (mg/g)	K_L (L/mg)	R^2	R_L	$1/n$	K_F ($mg^{1-n} L^n/g$)	R^2
298	680.2	0.088	0.999	0.102	0.349	143.0	0.927
308	769.2	0.084	0.999	0.106	0.338	167.9	0.973
318	833.3	0.077	0.997	0.114	0.336	159.9	0.952

The calculated Q_m in the Langmuir model is 680.2 mg/g, much bigger than many other materials (Table 4). $1/n$ values from the Freundlich isotherm are all less than 0.35, indicating that relatively high adsorption intensity occurred [10].

Table 4. Comparison of Hg²⁺ removal capability.

Adsorbent	pH	Fitting Models	Q _m (mg/g)	Ref.
Titanate nanotube adsorbents	10	Sips	140	[41]
Lignocellulosic	5	Langmuir	28	[42]
Modified magnetic chitosan	5	Langmuir	96	[43]
NH ₂ -CoFe ₂ O ₄ -chitosan-graphene	7	Langmuir	361	[44]
functionalized Carbon nanotubes	5.5	Freundlich	186.97	[45]
Polypyrrole multilayer cellulose	6	Langmuir	31.68	[46]
Poly (2-aminothiazole)	6.5	Langmuir	325.7	[47]
CoFe ₂ O ₄ @SiO ₂ -NH ₂	7	Langmuir	149.3	[10]
Short channel SBA-15-SH	8	Freundlich	195.6	[48]
CoFe ₂ O ₄ @SiO ₂ -Ppy	8	Langmuir	680.2	This work

By comparison, the Freundlich model has a poor fitting degree with R^2 below 0.98. Therefore, the adsorption process of CoFe₂O₄@SiO₂-Ppy for Hg²⁺ is more suitably depicted by the Langmuir model.

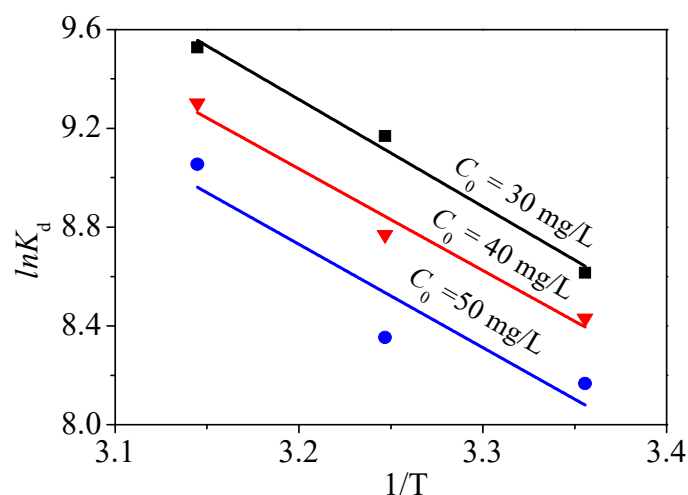
3.5. Adsorption Thermodynamics

Thermodynamic parameters of Gibbs free energy (ΔG^0 , kJ/mol), enthalpy (ΔH^0 , kJ/mol) and entropy (ΔS^0 , kJ/(mol·K)) can be used to analyze the thermodynamics based on the following equations:

$$\Delta G^0 = -RT \ln K_d \quad (7)$$

$$\ln K_d = \frac{\Delta S^0}{R} - \frac{\Delta H^0}{RT} \quad (8)$$

here, R is 8.314 J/(mol·K). K_d represents thermodynamic constant. Data obtained by $\ln K_d$ versus $1/T$ is plotted and fitted to calculate ΔH^0 and ΔS^0 based on the slopes and intercepts of fitted plot. The results are exhibited in Figure 14 and Table 5.

**Figure 14.** Linear fitting of thermodynamics.**Table 5.** Thermodynamic parameters.

C ₀	ΔH^0	ΔS^0	ΔG^0		
			298 K	308 K	318 K
30	0.036	192.763	-21.346	-23.480	-25.422
40	0.035	184.635	-20.890	-22.457	-24.594
50	0.034	183.725	-20.235	-21.392	-23.941

The three positive ΔH^0 values suggest that Hg^{2+} removal is endothermic. Negative ΔG^0 values indicate a spontaneous adsorption and some chemical processes are involved [10], which is consistent with the analysis from adsorption isotherms. The positive ΔS^0 values illustrate that a disorderly solid–solution interface and high temperature are favorable to the removal of Hg^{2+} by $\text{CoFe}_2\text{O}_4@/\text{SiO}_2\text{-Ppy}$ [10,48].

3.6. Effect of Coexistence Ions

Natural water or industrial wastewater commonly contains various metal ions. These metal ions can affect on the adsorption of mercury through competing with Hg^{2+} for adsorption. Consequently, it is necessary to use $\text{CoFe}_2\text{O}_4@/\text{SiO}_2\text{-Ppy}$ to survey the aggressive effect of ionic strength and coexisting ions on the ability of $\text{CoFe}_2\text{O}_4@/\text{SiO}_2\text{-Ppy}$.

One hundred mL Hg^{2+} solution containing six common ions (Cl^{-1} , NO_3^{-} , SO_4^{2-} , Na^+ , K^+ , and Ca^{2+}) with different concentrations (0 mM, 10 mM, and 100 mM) was contacted with $\text{CoFe}_2\text{O}_4@/\text{SiO}_2\text{-Ppy}$ (5 mg) at pH = 8 for 8 h. After the reaction, the residual content of Hg^{2+} was measured, and the corresponding data are shown in Figure 15.

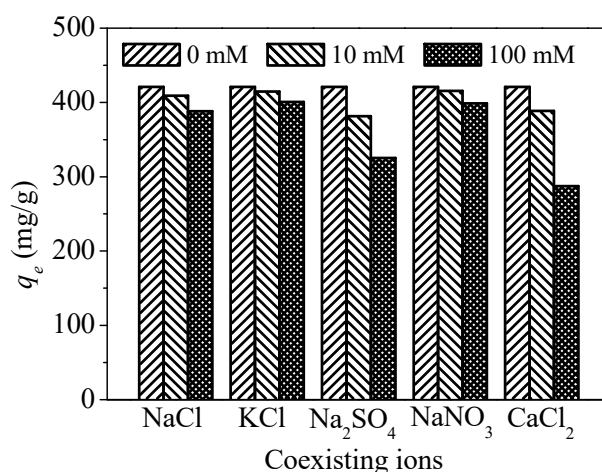


Figure 15. Effect of coexisting ions.

As ionic concentration increases, the adsorption capacity of $\text{CoFe}_2\text{O}_4@/\text{SiO}_2\text{-Ppy}$ for Hg^{2+} decreases. Among the three anions (Cl^{-1} , NO_3^{-} , SO_4^{2-}), SO_4^{2-} has a greater impact on the removal of Hg^{2+} , and the removal efficiencies decrease by 9.29% and 22.74% at the concentrations of 10 mM and 100 mM, respectively. It may be because the amino group has a higher affinity for SO_4^{2-} than Cl^{-1} and NO_3^{-} [22].

Among these cations (Na^+ , K^+ , Ca^{2+}), Ca^{2+} generates a large influence on the adsorption, and the capacity for Hg^{2+} removal is reduced by 13.12% and 31.73% at the concentrations of 10 mM and 100 mM, respectively. It may be because Ca^{2+} is a divalent cation and occupies two active adsorption sites [49].

3.7. Application Evaluation

In practical application, the adsorption and desorption performances are two key indices for judging an adsorbent. An ideal adsorbent should have a high adsorbability. In addition, it is also important to have a good regeneration capacity, so that the material can be reused many times, thus greatly reducing the disposal cost.

It can be seen from the above experiments that changes in pH significantly affect the adsorption process of $\text{CoFe}_2\text{O}_4@/\text{SiO}_2\text{-Ppy}$ for Hg^{2+} . As pH increases, the adsorption capacity increases in the pH range 3–9. Thus, the desorption of $\text{CoFe}_2\text{O}_4@/\text{SiO}_2\text{-Ppy}$ can be achieved by pickling with an acidic solution [48]. 0.005 g of $\text{CoFe}_2\text{O}_4@/\text{SiO}_2\text{-Ppy}$ was first contacted with 100 mL Hg^{2+} solution (40 mg/L)

for 8 h at 298 K. The resulting Hg^{2+} -adsorbed $\text{CoFe}_2\text{O}_4@\text{SiO}_2\text{-Ppy}$ composite was filtered and then eluted with 100 mL 0.2 mol/L HCl solution. The whole process was repeated 5 times. The experimental results are exhibited in Figure 16.

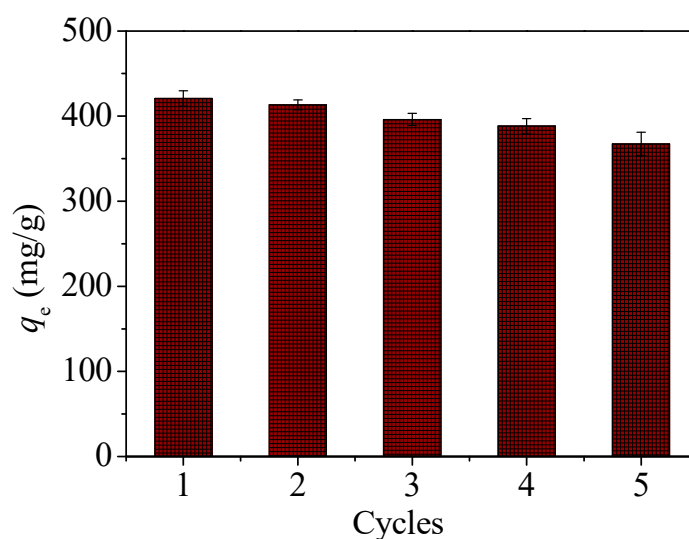


Figure 16. Adsorption and regeneration cycles of $\text{CoFe}_2\text{O}_4@\text{SiO}_2\text{-Ppy}$.

After five cycles, the capacity of $\text{CoFe}_2\text{O}_4@\text{SiO}_2\text{-Ppy}$ for Hg^{2+} only decreased by 12.7% and still reached 367.3 mg/g. This shows that $\text{CoFe}_2\text{O}_4@\text{SiO}_2\text{-Ppy}$ is a promising heavy metal adsorption material.

To further assess the performance of $\text{CoFe}_2\text{O}_4@\text{SiO}_2\text{-Ppy}$, electroplating wastewater was used as the target to be processed. In the test, the employed metal ions in the electroplating wastewater included Hg^{2+} (2.2 mg/L), Cr^{3+} (3.2 mg/L), Ni^{2+} (2.3 mg/L), Cu^{2+} (0.9 mg/L), and Cd^{2+} (2.5 mg/L). The Chemical Oxygen Demand was 76.6 mg/L. The used amount of adsorbent was 0.1 g/L.

The result shows that the efficiency E (%) achieved over 99.6% and the residual content of Hg^{2+} ions was below 0.05 mg/L, meeting the effluent standard of “Emission Standard of Pollutants for Electroplating” (GB 21900-2008). Based on the applied result, it has been demonstrated that $\text{CoFe}_2\text{O}_4@\text{SiO}_2\text{-Ppy}$ is a valuable and promising adsorbent.

3.8. Mechanism Speculation

It is well known that mercury has a variety of forms in aqueous solutions, including Hg^{2+} , HgOH^+ , HgCl^+ , and $\text{Hg}(\text{OH})_2$ [48], etc. Under acidic conditions ($\text{pH} < 3$), mercury in solution is mainly in the forms of Hg^{2+} , HgOH^+ , and $\text{Hg}(\text{OH})_2$ [48]. The formation of Hg^{2+} is the main morphology as the pH increases, and dissolved $\text{Hg}(\text{OH})_2$ gradually becomes the main morphology when pH is more than 6 [13].

Adsorption of Hg^{2+} with $\text{CoFe}_2\text{O}_4@\text{SiO}_2\text{-Ppy}$ is a process affected by pH. As the pH increases, the effect becomes greater. HgOH^+ , HgCl^+ , and $\text{Hg}(\text{OH})_2$ are abundant in the solution under alkaline conditions, and these ions are more easily adsorbed onto $\text{CoFe}_2\text{O}_4@\text{SiO}_2\text{-Ppy}$ due to their better size and higher mobility compared to Hg^{2+} [50].

The main adsorption site of Hg^{2+} is the N atom in the polypyrrole chain. Heavy metal ions can share solitary electrons with the N atom in the $-\text{N}=\text{C}-$ group [51], as the N atom has a pair of electrons, which can form a complex with Hg^{2+} ions.

When $\text{pH} < 5$, the pair of electrons on the nitrogen is slightly protonated, hindering the formation of complexes. When the pH is at the range of 5–10, the main form of mercury is dissolved $\text{Hg}(\text{OH})_2$, able to form a stable structure of the complex with the pair of electrons on the nitrogen, causing a high removal of Hg^{2+} by $\text{CoFe}_2\text{O}_4@\text{SiO}_2\text{-Ppy}$.

Figure 17a shows the XPS patterns of $\text{CoFe}_2\text{O}_4@\text{SiO}_2\text{-Ppy}$. After adsorption, the intensities of C 1s, N 1s, O 1s, and Si 2p in $\text{CoFe}_2\text{O}_4@\text{SiO}_2\text{-Ppy-Hg}$ are reduced and new Hg 4f and Hg 4p appear. There are two peaks at 101.2 and 105.3 eV in Figure 17b, attributed to Hg 4f_{5/2} and Hg 4f_{7/2}, respectively, and another peak at 102.9 eV is Si 2p [13]. In Figure 17c, due to the adsorption of Hg^{2+} , the whole of the N peak is shifted and the shifted value is approximately at 1 eV [52].

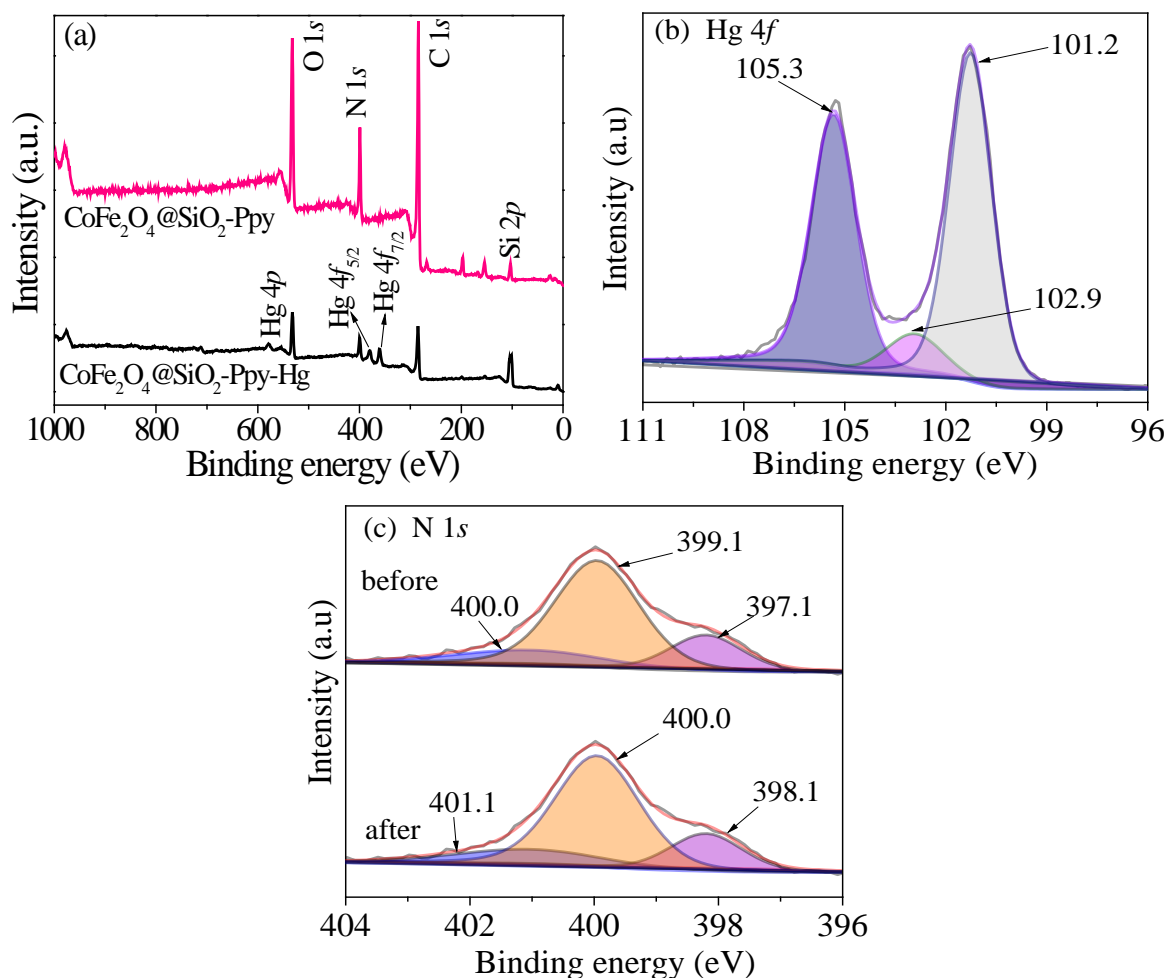


Figure 17. XPS patterns of (a) survey scan, (b) Hg 4f and (c) N 1s.

The results indicate that a chemical reaction is involved in the adsorption of Hg^{2+} onto $\text{CoFe}_2\text{O}_4@\text{SiO}_2\text{-Ppy}$, which is consistent with the isotherm and thermodynamic analyses. XPS analysis directly proves that Hg^{2+} ions have been successfully attached to the surface of $\text{CoFe}_2\text{O}_4@\text{SiO}_2\text{-Ppy}$.

4. Conclusions

A new polypyrrole-grafted magnetic compound, $\text{CoFe}_2\text{O}_4@\text{SiO}_2\text{-Ppy}$, was successfully synthesized with a facile hydrothermal method under relatively safe conditions. $\text{CoFe}_2\text{O}_4@\text{SiO}_2\text{-Ppy}$ can effectively adsorb Hg^{2+} ions from water. The fittings of kinetics, isotherms, and thermodynamics showed the adsorption of Hg^{2+} was endothermic and spontaneous, and involved some chemical reactions. The value of Q_m from the Langmuir model reached 680.2 mg/g, exceeding that of many adsorbents. In addition, $\text{CoFe}_2\text{O}_4@\text{SiO}_2\text{-Ppy}$ had excellent regeneration ability, dispersibility, and stability. The application results show that $\text{CoFe}_2\text{O}_4@\text{SiO}_2\text{-Ppy}$ can be an excellent adsorbent for removing heavy metal ions from aqueous solutions.

Author Contributions: Data curation, Y.Z., K.X., Z.Z. (Zhenzong Zhang), Z.Z. (Ziming Zhu) and Z.Q.; Investigation, Y.Z.; Project administration, Y.G.; Supervision, Y.G.; Writing—original draft, Y.Z.; Writing—review & editing, Y.G.

Funding: This research was supported by the National Natural Science Foundation of China grant number (51578354), Jiangsu Provincial Key Laboratory of Environmental Science and Engineering grant number (Zd201705), Natural Science Research Project of Jiangsu Province Higher Education (18KJA610002), Six Talent Peaks Program (2016-JNHB-067) and Qing Lan Project of Jiangsu Province.

Conflicts of Interest: The authors declare no conflict of interest. The founding sponsors had no role in the design of the study; in the collection, analyses, or interpretation of data; in the writing of the manuscript, and in the decision to publish the results.

References

1. Azimi, A.; Azari, A.; Rezakazemi, M.; Ansarpour, M. Removal of heavy metals from industrial wastewaters: A review. *Chem. Biol. Eng. Rev.* **2017**, *4*, 37–59. [[CrossRef](#)]
2. Branco, V.; Caito, S.; Farina, M.; Teixeira, d.R.J.; Aschner, M.; Carvalho, C. Biomarkers of mercury toxicity: Past, present, and future trends. *J. Toxicol. Environ. Health B* **2017**, *20*, 119–154. [[CrossRef](#)] [[PubMed](#)]
3. Xu, H.; Jia, J.; Guo, Y.; Qu, Z.; Liao, Y.; Xie, J.; Shangguan, W.; Yan, N. Design of 3D MnO₂/Carbon sphere composite for the catalytic oxidation and adsorption of elemental mercury. *J. Hazard. Mater.* **2018**, *342*, 69–76. [[CrossRef](#)] [[PubMed](#)]
4. Hadi, P.; To, M.H.; Hui, C.W.; Lin, C.S.K.; McKay, G. Aqueous mercury adsorption by activated carbons. *Water Res.* **2015**, *73*, 37–55. [[CrossRef](#)] [[PubMed](#)]
5. Kumar, A.; Subudhi, S. Preparation, characteristics, convection and applications of magnetic nanofluids: A review. *Heat Mass Transf.* **2017**, *54*, 241–265. [[CrossRef](#)]
6. Haneda, K.; Morrish, A.H. Noncollinear magnetic structure of CoFe₂O₄ small particles. *J. Appl. Phys.* **1988**, *63*, 4258–4260. [[CrossRef](#)]
7. Roto, R.; Yusran, Y.; Kuncaka, A. Magnetic adsorbent of Fe₃O₄@SiO₂ core-shell nanoparticles modified with thiol group for chloroauric ion adsorption. *Appl. Surf. Sci.* **2016**, *377*, 30–36. [[CrossRef](#)]
8. Ren, C.; Ding, X.; Fu, H.; Meng, C.; Li, W.; Yang, H. Preparation of amino-functionalized CoFe₂O₄@SiO₂ magnetic nanocomposites for potential application in absorbing heavy metal ions. *RSC Adv.* **2016**, *6*, 72479–72486. [[CrossRef](#)]
9. Zhou, Q.; Li, J.; Wang, M.; Zhao, D. Iron-based magnetic nanomaterials and their environmental applications. *Crit. Rev. Environ. Sci. Technol.* **2016**, *46*, 783–826. [[CrossRef](#)]
10. Wang, X.; Zhang, Z.; Zhao, Y.; Xia, K.; Guo, Y.; Qu, Z.; Bai, R. A mild and facile synthesis of amino functionalized CoFe₂O₄@SiO₂ for Hg(II) removal. *Nanomaterials* **2018**, *8*, 673. [[CrossRef](#)]
11. Huang, X.; Yang, J.Y.; Wang, J.K.; Bi, J.T.; Xie, C.; Hao, H.X. Design and synthesis of core-shell Fe₃O₄@PTMT composite magnetic microspheres for adsorption of heavy metals from high salinity wastewater. *Chemosphere* **2018**, *206*, 513–521. [[CrossRef](#)]
12. Zhang, S.; Zhang, Y.; Liu, J.; Xu, Q.; Xiao, H.; Wang, X.; Xu, H.; Zhou, J. Thiol modified Fe₃O₄@SiO₂ as a robust, high effective, and recycling magnetic sorbent for mercury removal. *Chem. Eng. J.* **2013**, *225*, 30–38. [[CrossRef](#)]
13. Zhu, H.; Shen, Y.; Wang, Q.; Chen, K.; Wang, X.; Zhang, G.; Yang, J.; Guo, Y.; Bai, R. Highly promoted removal of Hg(II) with magnetic CoFe₂O₄@SiO₂ core-shell nanoparticles modified by thiol groups. *RSC Adv.* **2017**, *7*, 39204–39215. [[CrossRef](#)]
14. Song, B.Y.; Eom, Y.; Lee, T.G. Removal and recovery of mercury from aqueous solution using magnetic silica nanocomposites. *Appl. Surf. Sci.* **2011**, *257*, 4754–4759. [[CrossRef](#)]
15. Gharagozlou, M.; Ramezanzadeh, B.; Baradaran, Z. Synthesize and characterization of a novel anticorrosive cobalt ferrite nanoparticles dispersed in silica matrix (CoFe₂O₄-SiO₂) to improve the corrosion protection performance of epoxy coating. *Appl. Surf. Sci.* **2016**, *377*, 86–98. [[CrossRef](#)]
16. Wang, S.; Wang, K.; Dai, C.; Shi, H.; Li, J. Adsorption of Pb²⁺ on amino-functionalized core-shell magnetic mesoporous SBA-15 silica composite. *Chem. Eng. J.* **2015**, *262*, 897–903. [[CrossRef](#)]
17. Ren, C.; Ding, X.; Fu, H.; Li, W.; Wu, H.; Yang, H. Core-shell superparamagnetic monodisperse nanospheres based on amino-functionalized CoFe₂O₄@SiO₂ for removal of heavy metals from aqueous solutions. *RSC Adv.* **2017**, *7*, 6911–6921. [[CrossRef](#)]

18. Hozhabr Araghi, S.; Entezari, M.H. Amino-functionalized silica magnetite nanoparticles for the simultaneous removal of pollutants from aqueous solution. *Appl. Surf. Sci.* **2015**, *333*, 68–77. [[CrossRef](#)]
19. Qi, H.; Wang, S.; Liu, H.; Gao, Y.; Wang, T.; Huang, Y. Synthesis of an organic–inorganic polypyrrole/titanium(IV) biphosphate hybrid for Cr(VI) removal. *J. Mol. Liq.* **2016**, *215*, 402–409. [[CrossRef](#)]
20. Zhou, C.; Zhu, H.; Wang, Q.; Wang, J.; Cheng, J.; Guo, Y.; Zhou, X.; Bai, R. Adsorption of mercury(II) with an Fe₃O₄ magnetic polypyrrole-graphene oxide nanocomposite. *RSC Adv.* **2017**, *7*, 18466–18479. [[CrossRef](#)]
21. Sun, S.; Zeng, H.; Robinson, D.B.; Raoux, S.; Rice, P.M.; Wang, S.X.; Li, G. Monodisperse MFe₂O₄ (M = Fe, Co, Mn) nanoparticles. *J. Am. Chem. Soc.* **2004**, *126*, 273–279. [[CrossRef](#)] [[PubMed](#)]
22. Wang, H.; Yuan, X.; Wu, Y.; Chen, X.; Leng, L.; Wang, H.; Li, H.; Zeng, G. Facile synthesis of polypyrrole decorated reduced graphene oxide–Fe₃O₄ magnetic composites and its application for the Cr(VI) removal. *Chem. Eng. J.* **2015**, *262*, 597–606. [[CrossRef](#)]
23. Bhaumik, M.; Leswif, T.Y.; Maity, A.; Srinivasu, V.V.; Onyango, M.S. Removal of fluoride from aqueous solution by polypyrrole/Fe₃O₄ magnetic nanocomposite. *J. Hazard. Mater.* **2011**, *186*, 150–159. [[CrossRef](#)] [[PubMed](#)]
24. Tripathi, K.M.; Castro, M.; Feller, J.-F.; Sonkar, S.K. Characterization of metal, semiconductor, and metal-semiconductor core–shell nanostructures. In *Metal Semiconductor Core–Shell Nanostructures for Energy and Environmental Applications*; Micro Nano Technologies; Elsevier: Amsterdam, The Netherlands, 2017; pp. 51–77.
25. Viltužnik, B.; Košak, A.; Zub, Y.L.; Lobnik, A. Removal of Pb(II) ions from aqueous systems using thiol-functionalized cobalt-ferrite magnetic nanoparticles. *J. Sol-Gel. Sci. Technol.* **2013**, *68*, 365–373.
26. Cheah, K.; Forsyth, M.; Truong, V.T. Ordering and stability in conducting polypyrrole. *Synth. Met.* **1998**, *94*, 215–219. [[CrossRef](#)]
27. Karthik, R.; Meenakshi, S. Synthesis, characterization and Cr(VI) uptake study of polyaniline coated chitin. *Int. J. Biol. Macromol.* **2015**, *72*, 235–242. [[CrossRef](#)]
28. Dong, S.; Dou, X.; Mohan, D.; Pittman, C.U., Jr.; Luo, J. Synthesis of graphene oxide/schwertmannite nanocomposites and their application in Sb(V) adsorption from water. *Chem. Eng. J.* **2015**, *270*, 205–214. [[CrossRef](#)]
29. Zhang, Y.; Xu, Q.; Zhang, S.; Liu, J.; Zhou, J.; Xu, H.; Xiao, H.; Li, J. Preparation of thiol-modified Fe₃O₄@SiO₂ nanoparticles and their application for gold recovery from dilute solution. *Sep. Purif. Technol.* **2013**, *116*, 391–397. [[CrossRef](#)]
30. Saucedo, I.S.; Munive, G.T.; Castro, T.D.C.; Vega, M.A.; Castillo, L.S.Q. Selective adsorption of metallic complex using polyaniline or polypyrrole. *Mater. Chem. Phys.* **2016**, *182*, 39–48. [[CrossRef](#)]
31. Amalraj, A.; Selvi, M.K.; Rajeswari, A.; Christy, E.J.S.; Pius, A. Efficient removal of toxic hexavalent chromium from aqueous solution using threonine doped polypyrrole nanocomposite. *J. Water Process Eng.* **2016**, *13*, 88–99. [[CrossRef](#)]
32. Bai, L.; Li, Z.; Zhang, Y.; Wang, T.; Lu, R.; Zhou, W.; Gao, H.; Zhang, S. Synthesis of water-dispersible graphene-modified magnetic polypyrrole nanocomposite and its ability to efficiently adsorb methylene blue from aqueous solution. *Chem. Eng. J.* **2015**, *279*, 757–766. [[CrossRef](#)]
33. Tripathi, K.M.; Tuan Sang, T.; Kim, Y.J.; Kim, T. Green Fluorescent Onion-Like Carbon Nanoparticles from Flaxseed Oil for Visible Light Induced Photocatalytic Applications and Label Free Detection of Al(III) Ions. *ACS Sustain. Chem. Eng.* **2017**, *5*, 3982–3992. [[CrossRef](#)]
34. Lim, C.W.; Song, K.; Kim, S.H. Synthesis of PPy/silica nanocomposites with cratered surfaces and their application in heavy metal extraction. *J. Ind. Eng. Chem.* **2012**, *18*, 24–28. [[CrossRef](#)]
35. Larraza, I.; López-González, M.; Corrales, T.; Marcelo, G. Hybrid materials: Magnetite–Polyethyl enimine–Montmorillonite, as magnetic adsorbents for Cr(VI) water treatment. *J. Colloid Interface Sci.* **2012**, *385*, 24–33. [[CrossRef](#)] [[PubMed](#)]
36. Harijan, D.K.L.; Chandra, V.; Yoon, T.; Kim, K.S. Radioactive iodine capture and storage from water using magnetite nanoparticles encapsulated in polypyrrole. *J. Hazard. Mater.* **2018**, *344*, 576–584. [[CrossRef](#)] [[PubMed](#)]
37. Yang, Y.; Chen, N.; Feng, C.; Li, M.; Gao, Y. Chromium removal using a magnetic corncob biochar/polypyrrole composite by adsorption combined with reduction: Reaction pathway and contribution degree. *Colloid Surf. A* **2018**, *556*, 201–209. [[CrossRef](#)]

38. Zhou, J.; Lü, Q.-F.; Luo, J.-J. Efficient removal of organic dyes from aqueous solution by rapid adsorption onto polypyrrole-based composites. *J. Clean. Prod.* **2017**, *167*, 739–748. [[CrossRef](#)]
39. Abdi, S.; Nasiri, M.; Mesbahi, A.; Khani, M.H. Investigation of uranium (VI) adsorption by polypyrrole. *J. Hazard. Mater.* **2017**, *332*, 132–139. [[CrossRef](#)]
40. Ren, Y.; Abbood, H.A.; He, F.; Peng, H.; Huang, K. Magnetic EDTA-modified chitosan/SiO₂/Fe₃O₄ adsorbent: Preparation, characterization, and application in heavy metal adsorption. *Chem. Eng. J.* **2013**, *226*, 300–311. [[CrossRef](#)]
41. López-Muñoz, M.-J.; Arencibia, A.; Cerro, L.; Pascual, R.; Melgar, Á. Adsorption of Hg(II) from aqueous solutions using TiO₂ and titanate nanotube adsorbents. *Appl. Surf. Sci.* **2016**, *367*, 91–100. [[CrossRef](#)]
42. Arias Arias, F.E.; Beneduci, A.; Chidichimo, F.; Furia, E.; Straface, S. Study of the adsorption of mercury (II) on lignocellulosic materials under static and dynamic conditions. *Chemosphere* **2017**, *180*, 11–23. [[CrossRef](#)] [[PubMed](#)]
43. Azari, A.; Gharibi, H.; Kakavandi, B.; Ghanizadeh, G.; Javid, A.; Mahvi, A.H.; Sharafi, K.; Khosravia, T. Magnetic adsorption separation process: An alternative method of mercury extracting from aqueous solution using modified chitosan coated Fe₃O₄ nanocomposites. *J. Chem. Technol. Biotechnol.* **2017**, *92*, 188–200. [[CrossRef](#)]
44. Zhang, Y.; Yan, T.; Yan, L.; Guo, X.; Cui, L.; Wei, Q.; Du, B. Preparation of novel cobalt ferrite/chitosan grafted with graphene composite as effective adsorbents for mercury ions. *J. Mol. Liq.* **2014**, *198*, 381–387. [[CrossRef](#)]
45. Alomar, M.K.; Alsaadi, M.A.; Hayyan, M.; Akib, S.; Ibrahim, M.; Hashim, M.A. Allyl triphenyl phosphonium bromide based DES-functionalized carbon nanotubes for the removal of mercury from water. *Chemosphere* **2017**, *167*, 44–52. [[CrossRef](#)] [[PubMed](#)]
46. Hanif, Z.; Lee, S.; Qasim, G.H.; Ardiningsih, I.; Kim, J.A.; Seon, J.; Han, S.; Hong, S.; Yoon, M.H. Polypyrrole multilayer-laminated cellulose for large-scale repeatable mercury ion removal. *J. Mater. Chem. A* **2016**, *4*, 12425–12433. [[CrossRef](#)]
47. Wang, X.; Lv, P.; Zou, H.; Li, Y.; Li, X.; Liao, Y. Synthesis of Poly(2-aminothiazole) for Selective Removal of Hg(II) in Aqueous Solutions. *Ind. Eng. Chem. Res.* **2016**, *55*, 4911–4918. [[CrossRef](#)]
48. Shen, Y.; Jiang, N.; Liu, S.; Zheng, C.; Wang, X.; Huang, T.; Guo, Y.; Bai, R. Thiol functionalization of short channel SBA-15 through a safe, mild and facile method and application for the removal of mercury (II). *J. Environ. Chem. Eng.* **2018**, *6*, 5420–5433. [[CrossRef](#)]
49. Tran, L.; Wu, P.; Zhu, Y.; Yang, L.; Zhu, N. Highly enhanced adsorption for the removal of Hg(II) from aqueous solution by Mercaptoethylamine/Mercaptopropyltrimethoxysilane functionalized vermiculites. *J. Colloid Interface Sci.* **2015**, *445*, 348–356. [[CrossRef](#)] [[PubMed](#)]
50. Sun, Y.; Lv, D.; Zhou, J.; Zhou, X.; Lou, Z.; Baig, S.A.; Xu, X. Adsorption of mercury (II) from aqueous solutions using FeS and pyrite: A comparative study. *Chemosphere* **2017**, *185*, 452–461. [[CrossRef](#)] [[PubMed](#)]
51. Ghorbani, M.; Eisazadeh, H. Removal of COD, color, anions and heavy metals from cotton textile wastewater by using polyaniline and polypyrrole nanocomposites coated on rice husk ash. *Compos. Part B Eng.* **2013**, *45*, 1–7. [[CrossRef](#)]
52. Pan, S.; Zhang, Y.; Shen, H.; Hu, M. An intensive study on the magnetic effect of mercapto-functionalized nano-magnetic Fe₃O₄ polymers and their adsorption mechanism for the removal of Hg(II) from aqueous solution. *Chem. Eng. J.* **2012**, *210*, 564–574. [[CrossRef](#)]

